



On the Difference Between the Tensile Stiffness of Bulk and Slice Samples of Microstructured Materials

Rainer Glüge¹ · Holm Altenbach² · Nasir Mahmood³ · Mario Beiner³

Received: 21 July 2020 / Accepted: 28 September 2020 / Published online: 28 October 2020
© The Author(s) 2020, corrected publication 2021

Abstract

Many materials with a microstructure are statistically inhomogeneous, like casting skins in polymers or grain size gradients in polycrystals. It is desirable be able to account for the structural gradient. The first step is to measure the location dependent properties, for example by tensile testing of thin slices. Unfortunately, the slices properties can differ significantly from the bulk properties, since the slices lack a scale separation in one direction. For Polypropylen, we measured that Young's modulus of the slices is approximately 70% of the respective bulk value. We have identified three significant effects, all making the slices appear softer than the bulk material:

- *Load path confinement:* The approximate plane stress forces the load path through a softer phase where in 3D-of-plane load distribution is possible.
- *Free lateral straining:* In thin slices, small regions can contract freely, while phases have to contract concurrently in the bulk. Therefore, when two phases have very different Poisson ratios, the bulk appears stiffer than a slice.
- *Topological changes upon slicing:* Interpenetrating phases in the bulk can show features of a matrix-inclusion-structure in the slices.

We examine and quantify these effects in the linear elastic range for matrix-inclusion-structures and an interpenetrating-phase-structure. Some approaches on how the slice- vs bulk difference can be estimated are given.

✉ Rainer Glüge
gluege@uni-bremen.de

Holm Altenbach
holm.altenbach@ovgu.de

Nasir Mahmood
nasir.mahmood@imws.fraunhofer.de

Mario Beiner
mario.beiner@imws.fraunhofer.de

¹ University of Bremen, Bremen, Germany

² Otto-von-Guericke–University, Magdeburg, Germany

³ Fraunhofer Institute for Microstructure of Materials and Systems IMWS, Halle, Germany

Keywords Stiffness · Homogenization · Plane stress · Elasticity · Micro structure · Layers

1 Introduction

With the advancement of analytic and simulation tools, it becomes feasible to account for structural gradients and statistical inhomogeneous microstructures in engineering parts. Today, methods for optimizing a microstructure w.r.t. desired effective material properties are established, and textbook knowledge is available [1, 10]. The next step is to do such adjustments locally, as for example in [2] who optimized the local material distribution of a structure. A more recent example is the work of [6] who optimized the density of a polymer lattice in a cantilever beam. By this method, gradient structures are the result of a design process to enhance a part's functionality, but they also occur unintentional, for example as casting skins in polymers [15] or grain size gradients in metals [14].

To set up simulation models of such parts, the local material parameters are needed. To test the material locally, one might try to cut small samples. Unfortunately, these behave different from the bulk material, since the sliced samples lack a scale separation in one direction. This is also known from elastic homogenization. If the virtual samples (RVE-representative volume elements) are not large enough, i.e., not representative, the effective stiffness is underestimated when homogeneous stress boundary conditions are used, and overestimated when homogeneous strain boundary conditions are used. The kinematic constraints of homogeneous strains along the boundary cause reaction stresses additionally to the stresses inside the RVE, hence the stresses are overestimated and the material appears stiffer. On the other hand, homogeneous stress boundary conditions, like a traction-free surface in a tensile test, correspond to a minimum of kinematic constraints and hence a minimum of reaction stresses, so they underestimate the effect of embedding the RVE in a similar material. For RVE that tessellate, periodic boundary conditions mimic the embedding, and are exact for periodic microstructures but impose otherwise an artificial periodicity frame. The traction-free surfaces in tensile tests correspond to the homogeneous stress case, hence the slices appear softer in tensile tests. In general, the boundary influence vanishes upon increasing the RVE edge length l . Typically, a hyperbolic $1/l$ -convergence towards the effective properties is observed as l is increased, see e.g. [18] Fig. 3a or [7] Fig. 4 and 5, among many others. This is because the RVE volume grows with l^3 while the RVE boundary grows with l^2 . The RVE aspect ratios are usually kept constant, and convergence is rarely examined for individual RVE dimensions, although this offers some interesting perspectives. For example in thin wires with $l_1 \ll l_3$ and $l_2 \ll l_3$, Young's modulus along the l_3 -direction is just the Reuss¹ (harmonic) average of the individual phases' Young's moduli, since the load flows serial through the phases. The 2D tensile stiffness is intermediate between the 1D Reuss average and the 3D stiffness, i.e.

$$E_{1D} < E_{2D} < E_{3D} \quad (1)$$

holds. A sketch is given in Fig. 1. The ordering can be understood intuitively: At an interface, the material arrangement is serial along the one interface normal \mathbf{n} and parallel in the $D - 1$ directions parallel to the interface. The more dimensions D , the closer is the effective elasticity to the Voigt (arithmetic) average [24], while in the $D = 1$ case the effective

¹[20] proposed a homogeneous stress field in a different context, but in homogenization the term has been established for the harmonic mean of the stiffness, as it relies on the same assumption.

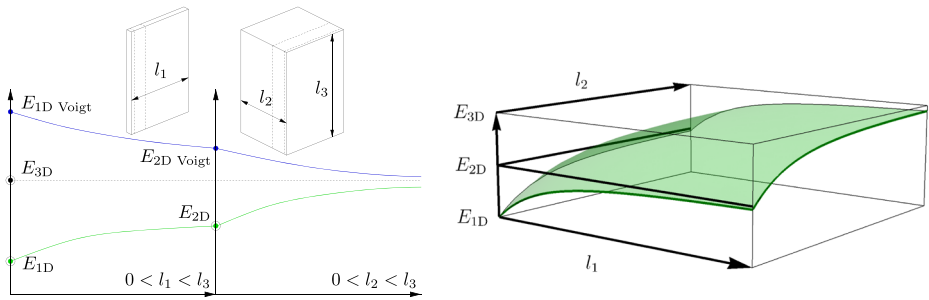


Fig. 1 Relation between sample dimensions l_1, l_2 and l_3 and convergence to 1D-, 2D- und 3D-Young-moduli (green) as limiting values $l_1 \ll l_3, l_2 \ll l_3$ (E_{1D}), $l_1 \ll l_3, l_2 \approx l_3$ (E_{2D}), $l_1 \approx l_2, l_2 \approx l_3$ (E_{3D}) in case of iso-stress boundary conditions (left image: lower curve) and iso-strain boundary conditions (left image: upper curve). The left part shows convergence from 1D to 2D when transitioning from a thin wire to a slice. The right part shows convergence from 2D to 3D, i.e. when the second cross-sectional extension is increased as well. The iso-stress boundary conditions correspond to traction free faces in tensile tests, which is why E_{1D} corresponds to the Reuss average of the Young-moduli. The encircled values are accessible by experiment. The iso-strain boundary conditions are practically impossible to realize experimentally, but can be imposed easily in simulations. On the right a sketch of the qualitative behaviour of the measured Young modulus is given depending on the cross sectional extensions l_1 and l_2

elasticity is the Reuss average, see [23]. Another homogenization result for lamellar structures with variable dimensions is given in [5].

Note that this effect can well be described in a purely classical, size-insensitive modelling framework, and does not require strain gradient modelling or micropolar approaches.

Contents of this article Firstly, we describe experimental findings for injection-molded polypropylene (PP) that clearly show the systematic difference between the 2D and the 3D properties (Sections 2 and 3).

The second part is devoted to the generation and analysis of synthetic data, which is obtained by mimicking the 2D and 3D tensile tests in FE simulations (Section 4).

In Section 5 we construct regressions for the 3D elasticity from this data. The statistical significance of the regression parameters allows to identify important contributions, which helped to identify the relevant softening effects due to slicing.

We finally make a proposal how the 2D to 3D difference can be accounted for at least in parts in well established estimates in Section 6.

2 Example 1: Sliced Polypropylene

Polymer parts exhibit a casting skin as depicted in Fig. 2. They are often used for thin-walled structures that undergo bending, which induces the largest strains near the surface. To accurately represent the loading in such parts, it is desirable to characterize the material properties layer-wise.

2.1 Sample Generation

Cuboid shaped specimens of dimensions 4 mm × 10 mm × 40 mm of a commercially available polypropylene (HJ120UB by Borealis) were produced by injection molding, with a melt temperature of 220 °C and an injection pressure of 195 bar (see [15] for more details).

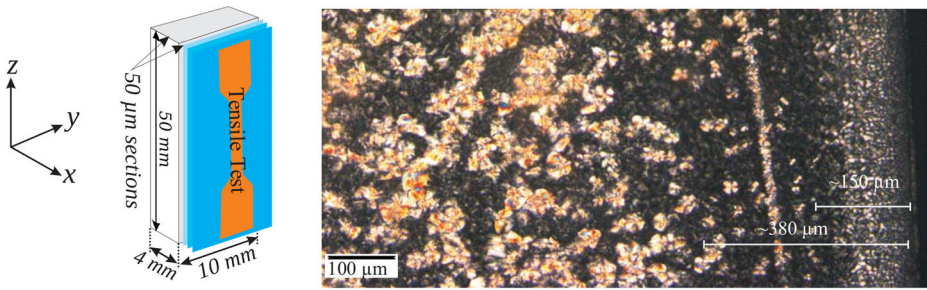


Fig. 2 Left: Geometry of an injection-molded PP sample for bending tests, the injection nozzle is at the center of the bottom plane. Right: micrograph inside the $x - z$ -plane showing skin (right) and core (left) structure of a typical injection molded PP sample

2.2 Tensile Testing of Bulk Specimen

The polymer block was clamped directly into a universal testing machine (Zwick/Roell Z010). The gauge length was assumed to be the clamping distance. The test speed was 27 mm/minute at a clamping distance of 27 mm, such that the nominal strain rate was $1/60 \text{ s}^{-1} \approx 0.0176 \text{ s}^{-1}$.

2.3 Tensile Testing of Thin Films

The injection molded bars were cut in the y - z -plane into slices of $50 \mu\text{m}$ by stepwise microtoming from the surface to the core via a Leica SM2500E sectioning system. The toming direction was the z -direction. Tensile specimens (shouldered test bars) were punched from these layers using a cutting-die unit according to ISO 527-2 Typ 5B. The positioning of the stencil was carefully adjusted to always cut the shouldered test strip at the same position. The specimen size was $6 \text{ mm} \times 35 \text{ mm}$, with a specimen gauge length of 12 mm. The tensile testing for the stress vs strain behavior was carried out on a Zwick universal testing machine (Z010, Zwick/Roell) at room temperature and a testing speed of 12 mm/min. The testing speeds were adjusted in proportion to the gauge length, such that the nominal strain rate was the same ($1/60 \text{ s}^{-1} \approx 0.0176 \text{ s}^{-1}$) for all tests.

A total of 40 slices was examined, from a depth of $25 \mu\text{m}$ (mid-plane) to $1975 \mu\text{m}$ in steps of $50 \mu\text{m}$. For each depth we averaged the results of at least 3 tests. For the largest sample set (7 slices) the standard deviation was less than 5% for Young's modulus. Some characteristic stress-strain curves are presented in Fig. 3 along with the fitted material model as detailed in the Section 2.4.

2.4 Material Model

We did not examine the strain rate dependence in more detail. The material properties depend on the depth. We found the deformation plasticity theory using the Ramberg-Osgood-relationship [19] to match the stress-strain behaviour up to approximately 10 % of strain quite well at all depths, see Fig. 3 for some representative stress-strain curves. The Ramberg-Osgood-law gives the strains as an explicit function of the stresses

$$\varepsilon = \frac{1}{E} \left[\sigma + \left(\frac{\sigma}{\sigma_y} \right)^n \right], \quad (2)$$

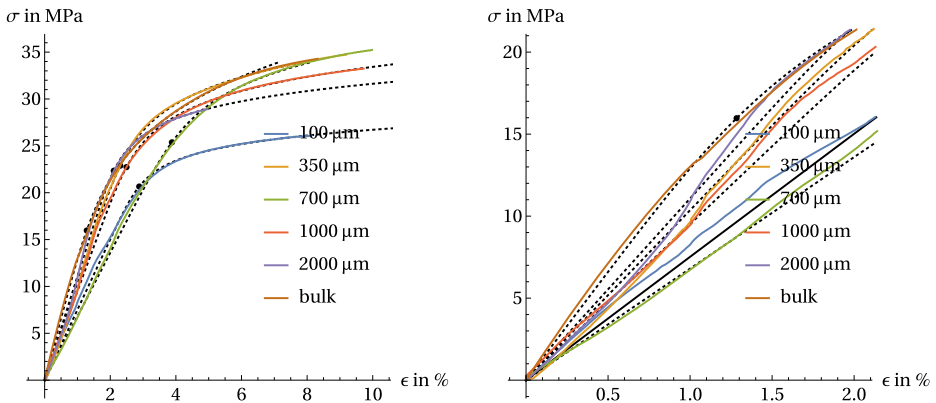


Fig. 3 Left: True stress over engineering strain curves obtained on thin sections at different depths, where the number indicates the starting depth of the layer (e.g., “100 μm” indicates the third layer, spanning the depth from 100 μm to 150 μm). The coloured solid lines correspond to the tensile test data, the black dotted lines represent the fitted material model (Eq. 2). The black dots indicate the yield point as obtained from fitting the Ramberg–Osgood material parameters. The bulk stress strain curve shows a higher stiffness and strength than most layers. Only at a depth of 350 μm, the bulk stress is exceeded in a small interval. Right: Zoom on the elastic portion. The bulk’s Young modulus is considerably larger than any of the Young moduli of the slices

where E is Young’s modulus, σ_y the yield stress and n the hardening exponent. The Ramberg–Osgood-model does not introduce plastic strains but is a nonlinear elasticity which mimics an elastic-plastic behavior, similar to the deformation theory of plasticity by [8] and [13]. Therefore, it cannot be applied if unloading or strain path changes occur.

Yield limit As can be seen in Fig. 3, no pronounced yield point is visible. In such cases, the yield point can be defined according to some rule, like the 0.2 % residual strain rule. For the Ramberg–Osgood law, the residual strain ϵ_{yres} after loading to σ_y is obtained by inserting $\sigma = \sigma_y$ and $\epsilon = \epsilon_{yres} + \sigma_y/E$,

$$\epsilon_{yres} = 1/E. \tag{3}$$

For our measurements of $E \approx 600$ MPa near the surface of the bulk sample to 1200 MPa well below the surface of the bulk sample, this corresponds to a residual strain between 0.083 % and 0.16 %, i.e., a reasonable yield point definition.

Hardening Note that larger values of n imply less hardening, hence the inverse hardening exponent $1/n$ actually quantifies the hardening. $1/n$ is the slope of the stress-strain-curve beyond the yield point in a double logarithmic plot.

Fitting the parameters E , σ_y and n to the experimental data The three parameters were fitted by the least squares method to the experimental data in the strain interval from 0 to 10 %, which is just before necking occurs in most of the tests. This was done for all layers between 25 μm (mid-plane) and 1975 μm in steps of 50 μm. The adopted material parameters are plotted over the depth in Fig. 4. One can see that on the surface, stiffness, yield strength and hardening have a local minimum. Conversely, approximately 300 μm below the surface, Young’s modulus and the inverse hardening exponent have a local maximum, while the yield stress remains roughly the same. At approximately 700 μm below the surface, Young’s modulus has a local minimum, the yield stress a local maximum and the

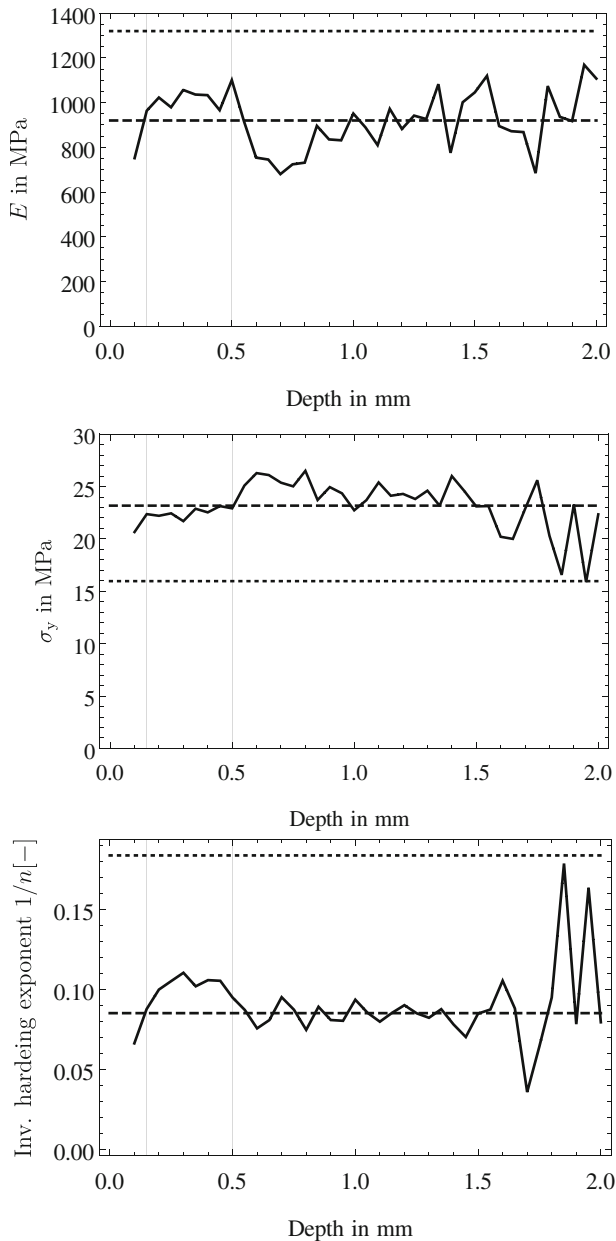


Fig. 4 Young's modulus E , the yield stress σ_y and the inverse hardening exponent $1/n$ over the depth in mm as fitted to the tensile test data (solid line) and on average (dashed line). The dotted line corresponds to the value for the bulk sample. One can see that the slice average differs significantly from the bulk values. The vertical lines at depths of 0.15 mm and 0.5 mm indicate the surface layer transitions between surface, shear zone and core

inverse hardening exponent drops to approximately 0.08. Since the core material is more brittle, there is an increased scattering of the results.

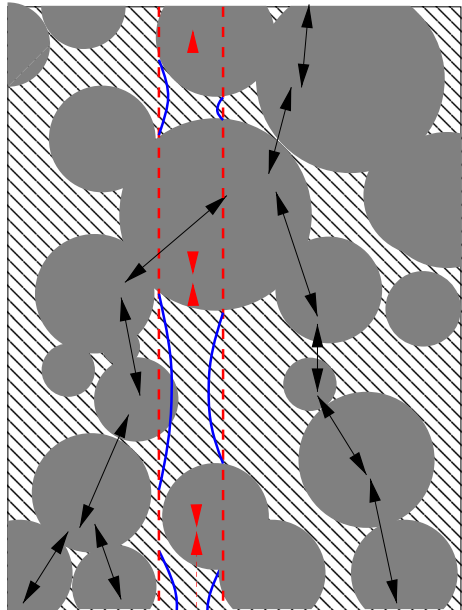
2.5 Layer Properties vs Bulk Properties

The layer-wise stiffnesses and yield limits are somewhat lower than the bulk properties of polypropylene. Young's modulus lies usually between 1300 MPa and 1800 MPa [9], the yield stress lies mostly between 25 MPa and 35 MPa [22]. Here, the average Young modulus of the layers is approximately 920 MPa, while the bulk's Young modulus is approximately 1320 MPa. Hence, the elastic properties are underestimated by a factor of approximately 0.7, see Fig. 3 right.

Similar observations hold for the plastic properties. We found the bulk sample to have a yield limit of only 16 MPa in comparison to an average around 23 MPa in the slices, and a high inverse hardening exponent of 0.18 in comparison to an average of around 0.09 in the slices, see Fig. 4.

Another finding is an increased scattering in the slices near the core (Fig. 4), which contains large spherulites. These approach the slice's thickness of $50\ \mu\text{m}$ (see Fig. 2). Near the surface, a finer microstructure prevails. Still, the variations do not exceed the bulk values. The semi-crystalline spherulites with a diameter of approximately $50\ \mu\text{m}$ are much stiffer than the amorphous matrix. In a bulk sample, the load path will go mostly through connected spherulites, (black arrows in Fig. 5). Upon sectioning, the load path is forced through the softer amorphous matrix (red arrows in Fig. 5). Additionally, the nearly incompressible amorphous matrix can freely contract in the slice (blue deformed shape in Fig. 5). Note that this is a size-independent effect.

Fig. 5 Lateral contraction and load path change upon slicing



3 Example 2: An Anisotropic Stiffness

3.1 Hooke’s law in 3 Dimensions

An anisotropic stiffness is characterized by a fourth order tensor \mathbb{C} that maps from the strains to the stresses or by the inverse mapping $\mathbb{S} = \mathbb{C}^{-1}$,

$$\sigma = \mathbb{C} : \varepsilon \qquad \varepsilon = \mathbb{S} : \sigma. \tag{4}$$

Here, the inverse always refers to the non-singular part of a tensor. For \mathbb{C} , this is in the space of fourth order tensors with the left and right subsymmetries, conveniently denoted as the inverse of the matrix in the normalized Voigt notation. W.r.t. an orthonormal basis e_i , the above scalar contractions become $\sigma_{ij} = C_{ijkl}\varepsilon_{kl}$ in indices, implying the usual summation over multiple indices. A suitable representation is the Kelvin-Mandel-basis²

$$B_1 = e_1 \otimes e_1 \quad B_2 = e_2 \otimes e_2 \qquad B_3 = \frac{1}{\sqrt{2}} (e_1 \otimes e_2 + e_2 \otimes e_1) \tag{5}$$

$$B_4 = e_3 \otimes e_3 \quad B_5 = \frac{1}{\sqrt{2}} (e_1 \otimes e_3 + e_3 \otimes e_1) \quad B_6 = \frac{1}{\sqrt{2}} (e_2 \otimes e_3 + e_3 \otimes e_2), \tag{6}$$

see e.g. [3] Sects. 26.2 and 26.3. The basis is normalized, such that the usual rules of calculus for matrices can be applied to corresponding component matrices. Note that we have chosen an ordering such that the components in the 1-2-plane are indexed from 1 to 3 while the components of the 1-2-plane are indexed from 4 to 6. This allows for a block-matrix separation of the in-plane and-of-plane parts of the stresses, strains and constitutive tensors \mathbb{C} and \mathbb{S} . Hooke’s law is then a matrix-vector product w.r.t. this basis.

$$\begin{bmatrix} \sigma_1 \\ \sigma_2 \\ \sigma_3 \\ \sigma_4 \\ \sigma_5 \\ \sigma_6 \end{bmatrix} = \begin{bmatrix} C_{11} & C_{12} & C_{13} & C_{14} & C_{15} & C_{16} \\ & C_{22} & C_{23} & C_{24} & C_{25} & C_{26} \\ & & C_{33} & C_{34} & C_{35} & C_{36} \\ \hline & & & C_{44} & C_{45} & C_{46} \\ & & & & C_{55} & C_{56} \\ \text{sym} & & & & & C_{66} \end{bmatrix} \begin{bmatrix} \varepsilon_1 \\ \varepsilon_2 \\ \varepsilon_3 \\ \varepsilon_4 \\ \varepsilon_5 \\ \varepsilon_6 \end{bmatrix}, \tag{7}$$

or

$$\sigma_i = C_{ij}\varepsilon_j \quad \text{and} \quad \varepsilon_i = S_{ij}\sigma_j, \quad \text{with} \quad S_{ij} = C_{ij}^{-1}, \quad i, j = 1 \dots 6 \tag{8}$$

in indices, where the components are

$$\sigma_i = \sigma : B_i \tag{9}$$

$$\varepsilon_i = \varepsilon : B_i \tag{10}$$

$$C_{ij} = \mathbb{C} :: B_i \otimes B_j \tag{11}$$

$$S_{ij} = \mathbb{S} :: B_i \otimes B_j. \tag{12}$$

3.2 Restriction to Plane States

Conversions from 3D to plane stress or plane strain cases are dispersed in the literature for different symmetries. Here, in case of plane strains in the 1-2-plane we have $\varepsilon_4 = 0, \varepsilon_5 =$

²Mandel introduced the normalized basis in [16], but it has already been used in a convoluted way by Kelvin [21].

0, $\varepsilon_6 = 0$ and in case of plane stresses in the 1-2-plane we have $\sigma_4 = 0, \sigma_5 = 0, \sigma_6 = 0$. For the in-plane part it is then sufficient to consider the upper left 3×3 block matrix of C_{ij} in case of plane strains or of S_{ij} in case of plane stresses. We denote the truncation or projection to the 3×3 -block matrix by \mathcal{P} .

To calculate the 2D stiffness from the 3D stiffness in case of plane stresses, we need to invert firstly \mathbb{C} to obtain \mathbb{S} , truncate to the in plane part, and invert the remaining 3×3 -matrix to obtain the plane stress stiffness. The 3D to 2D transitions can be summarized as follows for the different cases:

	compliance	stiffness
plane stresses:	$S_{ij}^{2D} = \mathcal{P}(S_{ij})$	$C_{ij}^{2D} = (\mathcal{P}(C_{ij}^{-1}))^{-1}$ (13)
plane strains:	$S_{ij}^{2D} = (\mathcal{P}(S_{ij}^{-1}))^{-1}$	$C_{ij}^{2D} = \mathcal{P}(C_{ij})$. (14)

As one expects, the conversions from 3D to 2D are homogeneous of degree 1 in the elastic constants. Further, as a consequence of Cauchy’s interlacing theorem (see, e.g., [11]), for plane stresses the eigenvalues of the plane stiffness tensor are smaller than the eigenvalues of the 3D stiffness tensor, $\lambda_{\mathbb{C}^{\text{plane stress}}} \leq \lambda_{\mathbb{C}^{3D}}$, i.e. the stiffness is reduced. Conversely, for plane strains the eigenvalues of the plane compliance tensor are smaller than the eigenvalues of the 3D compliance tensor, $\lambda_{\mathbb{S}^{\text{plane strain}}} \leq \lambda_{\mathbb{S}^{3D}}$, i.e. the stiffness is increased. This increase in stiffness reflects the reaction stresses due to the kinematic constraint of plane deformations.

3.3 Reconstruction of the 3D Stiffness from Orthogonal Plane Stress Stiffnesses

The above considerations hold identically for homogeneous materials. For inhomogeneous materials, the plane stiffnesses of thin slices are smaller due to reasons given in the introduction. Nevertheless, reversing the projections to plane states as described above is possible: Having measured plane stiffnesses in three orthogonal planes, we can invert these on the 3×3 matrix space, reassemble the 3D compliance (i.e. reversing the truncation/projection), and take its inverse in the 6×6 matrix space to get an extrapolated 3D stiffness.

Luckily, [4] have performed exactly such RVE simulations for diamond/ β -SiC composite thin film RVE and RAE (representative area elements) as depicted in Fig. 6.

The microstructure has been obtained from measurements. The plane stress stiffnesses from the RAE simulations are

$$C^{e_1} = \begin{bmatrix} 408.6 & 78.1 & -0.6 \times \sqrt{2} \\ & 410 & -0.8 \times \sqrt{2} \\ \text{sym} & & 163.7 \times 2 \end{bmatrix} \mathbf{B}_{\{2,4,6\}} \otimes \mathbf{B}_{\{2,4,6\}} \tag{15}$$

$$C_1^{e_3} = \begin{bmatrix} 384.7 & 74.1 & 0 \times \sqrt{2} \\ & 428.7 & -0.3 \times \sqrt{2} \\ \text{sym} & & 158.6 \times 2 \end{bmatrix} \mathbf{B}_{\{2,1,3\}} \otimes \mathbf{B}_{\{2,1,3\}} \tag{16}$$

$$C_2^{e_3} = \begin{bmatrix} 382.9 & 74.1 & -1.4 \times \sqrt{2} \\ & 430.6 & -2.4 \times \sqrt{2} \\ \text{sym} & & 158.4 \times 2 \end{bmatrix} \mathbf{B}_{\{2,1,3\}} \otimes \mathbf{B}_{\{2,1,3\}}, \tag{17}$$

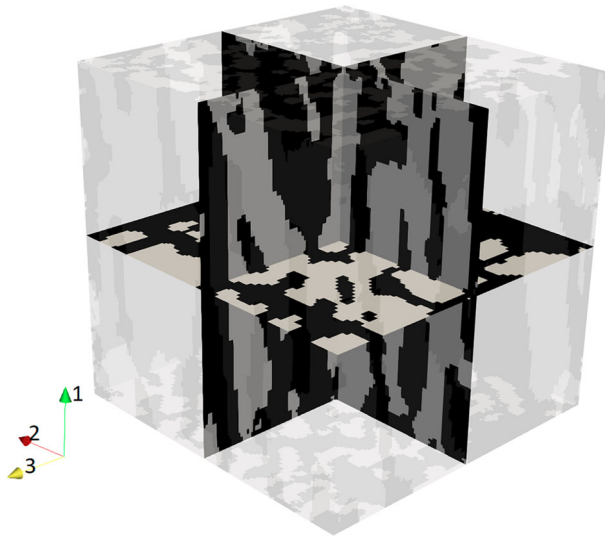


Fig. 6 3D RVE and three orthogonal 2D RAE, from [4]

with the index equal to the plane’s normal vector. The effective material is tetragonal: the 1-2 and the 1-3 planes exhibit equal effective properties. The given 3D stiffness from RVE simulations is

$$\mathbb{C} = \begin{bmatrix} 541.8 & 121.4 & 121.4 & 0 & 0 & 0 \\ & 482. & 119.1 & 0 & 0 & 0 \\ & & 482 & 0 & 0 & 0 \\ & & & 330.6 \times 2 & 0 & 0 \\ \text{sym} & & & & 347.4 \times 2 & 0 \\ & & & & & 347.4 \times 2 \end{bmatrix} \mathbf{B}_{\{1,2,4,6,5,3\}} \otimes \mathbf{B}_{\{1,2,4,6,5,3\}}, \quad (18)$$

see Table 9 [4]. All values are in GPa, we have added the normalizing factors of the Kelvin-Mandel-basis. We reassembled the 3D stiffness from the plane stress stiffnesses in the following way:

1. neglecting the almost zero components with absolute values below 3 GPa,
2. averaging the plane stiffnesses $\mathbb{C}_{1,2}^{e3}$ to $\mathbb{C}_{\text{transverse}}$.
3. inverting $\mathbb{C}_{\text{transverse}}$ and \mathbb{C}^{e1} to obtain the plane stress compliances,
4. reconstructing \mathbb{S}^{3D} from the latter, presuming the symmetry $\mathbb{S}_{\text{transverse}} = \mathbb{S}^{e2} = \mathbb{S}^{e3}$ (see Fig. 6).
5. inverting \mathbb{S}^{3D} to obtain \mathbb{C}^{3D} .

This procedure yields

$$\mathbb{C}^{\text{extrapolated}} = \begin{bmatrix} 453.5 & 98.8 & 99 & 0 & 0 & 0 \\ & 417.1 & 94.8 & 0 & 0 & 0 \\ & & 417.8 & 0 & 0 & 0 \\ & & & 327.4 \times 2 & 0 & 0 \\ \text{sym} & & & & 317 \times 2 & 0 \\ & & & & & 317 \times 2 \end{bmatrix} \mathbf{B}_{\{1,2,4,6,5,3\}} \otimes \mathbf{B}_{\{1,2,4,6,5,3\}}. \quad (19)$$

One can see that the extrapolated stiffness underestimates systematically the stiffness as measured on 3D RVE, with eigenvalue reductions between 1% and 16% w.r.t. the stiffness from the 3D RVE. Apparently, the lateral softening due to a lack of scale separation is at work. The difference is not as pronounced as in Section 2 because Poisson's ratios of the phases used in [4] are similar (0.2 vs. 0.17, see Table 1 in [4]).

4 Synthetic Data Generation

There are some potential problems with the measurements: The thin slices are prone to material modifications upon slicing, and minimal variations of the thickness may have a significant influence on the results. It is therefore not easy to separate the softening due to the loss of scale separation from other effects. To exclude such biases and examine the pure scale separation effect, we performed the same experiments numerically.

4.1 FE-Models

A simple bar of dimensions $10 \times 10 \times 50$ has been used as a tensile test sample. We have used a simple regular hexahedral mesh with quadratic shape functions and reduced integration (C3D20R in the Abaqus element library). The bulk has been meshed with $40 \times 40 \times 200 = 320000$ Elements. The total number of DOF is 4 000 083 in the 3D model. The material phases were assigned on the integration point level. The sliced samples with dimensions $10 \times 0.1 \times 50$ were cut directly from the bulk sample, with 171 609 DOF in $40 \times 1 \times 200 = 8000$ elements. Hence for each bulk sample we had 100 sliced samples. When talking about the effective properties of the slices, we always refer to the average over these 100 slices.

4.2 Microstructures

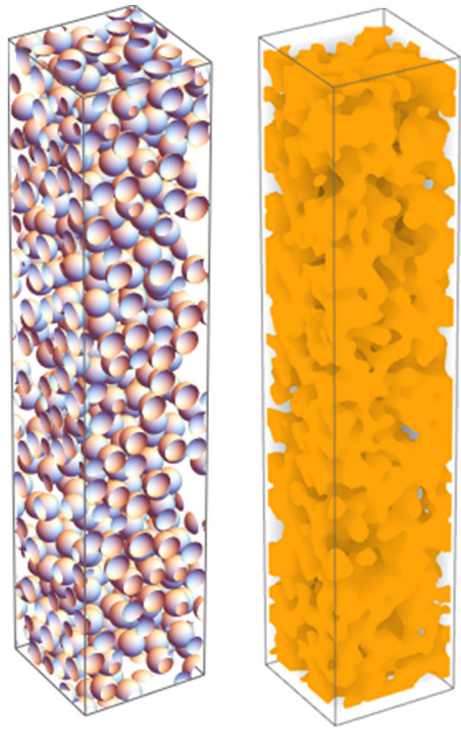
Firstly, a matrix with spherical inclusions with volume fractions 0.275, 0.358 and 0.5 has been studied. Secondly, a foam-like, symmetric, interpenetrating phase structure has been examined, see Fig. 7. Both structures are isotropic. The matrix inclusion structure has been generated by randomly dispersing spheres of uniform size for $v_{\text{inc}} = 0.275$ and $v_{\text{inc}} = 0.358$. For $v_{\text{inc}} = 0.5$ the spheres sizes needed to be reduced monotonically with increasing v_{inc} . The foam structure has been generated by a spinodal decomposition algorithm that is known to produce structures similar to a Cahn-Hilliard phase separation (see, e.g., [12]). We initialized a discrete lattice of dimensions $200 \times 200 \times 1000$ randomly with the values 0 or 1. Then, a Monte-Carlo evolution is applied, namely a flipping of the values according to the average in a surrounding $3 \times 3 \times 3$ cube. An average above 0.5 leads to the lattice value 1 and an average below 0.5 to the lattice value 0. The resulting structures appear to be isotropic, foam-like, and both phases have almost equal volume fractions.

4.3 Material Laws

We prescribed isotropic linear elasticity in the phases. Then, Hooke's law relates the deviatoric part $\boldsymbol{\varepsilon}' = \boldsymbol{\varepsilon} - \boldsymbol{\varepsilon}^\circ$ and the dilatoric part $\boldsymbol{\varepsilon}^\circ = \frac{\text{tr} \boldsymbol{\varepsilon}}{3} \mathbf{I}$ of the strain tensor $\boldsymbol{\varepsilon}$ individually to the same decomposition of the stresses $\boldsymbol{\sigma}$ by the shear modulus G and the compression modulus K ,

$$\boldsymbol{\sigma} = 3K \boldsymbol{\varepsilon}^\circ + 2G \boldsymbol{\varepsilon}'. \quad (20)$$

Fig. 7 The two structures “spherical inclusions” and interpenetrating phases (or “foam”) have been examined



One sees that the coefficients $3K$ and $2G$ are eigenvalues to the eigentensors $\boldsymbol{\varepsilon}^\circ$ (1D eigenspace) and $\boldsymbol{\varepsilon}'$ (5D eigenspace), which correspond to volumetric and shape-changing deformations, respectively. However, usually Young's modulus $E = \sigma_{\text{long}}/\varepsilon_{\text{long}}$ and Poisson's ratio $\nu = -\varepsilon_{\text{trans}}/\varepsilon_{\text{long}}$ are accessible in tensile tests, where the tensile direction is “long” and the transverse direction is “trans”. The following relationships hold between E , ν , K and G :

$$E = \frac{9KG}{3K + G} \quad (21)$$

$$\nu = \frac{3K - 2G}{6K + 2G} \quad (22)$$

$$K = \frac{E}{3(1 - 2\nu)} \quad (23)$$

$$G = \frac{E}{2(1 + \nu)}. \quad (24)$$

In our simulations, we considered all nontrivial combinations $K_{1,2} \in \{1, 10, 100\}$ MPa and $G_{1,2} \in \{1, 10, 100\}$ MPa. Trivial combinations are completely homogeneous composites like $K_1 = K_2$ and $G_1 = G_2$ simultaneously, which need not be considered. Additionally, the foam structure is due to the morphological symmetry invariant against interchanging the phase properties. This leads to 72 material combinations for each matrix-inclusion structure, i.e. regarding the three different volume fractions a total of 216 matrix-inclusion-samples, and 36 material combinations for the foam structure.

4.4 Results

4.4.1 Transition Behavior

We firstly examine the transition behavior of the effective Young’s modulus from the slice to the bulk properties for the material combination $K_{inc} = 10$ MPa, $G_{inc} = 10$ MPa, $K_{matrix} = 10$ MPa, $G_{matrix} = 1$ MPa in the matrix-inclusion-structure with $v_{inc} = 0.36$. We looked at thicknesses $t=0.1$ mm (100), 0.2 mm (50), 0.4 mm (25), 0.8 mm (12), 1.6 mm (6), 3.2 mm (3), 6.4 mm (1) and 10 mm (1) with the number of sample realizations given in brackets. All slices results are averages. The outcome is plotted with a regression in Fig. 8. As a regression we use

$$E = E_{bulk} + \frac{E_{-1}}{a + t} + \frac{E_{-2}}{(b + t)^2}, \tag{25}$$

where the parameter E_{bulk} is the asymptotic bulk modulus obtained for $t \rightarrow \infty$, the second term captures the main asymptotic behavior and the third term corrects the asymptotic towards $t \rightarrow 0$ when the thickness is much smaller than the inclusions. From the regression we obtain an effective Young’s modulus of 5.12 MPa for a thin slice and 6.5 MPa for the bulk. One obtains the ratio $E_{2D}/E_{3D} \approx 0.79$ for this particular microstructure. $E_{1D} = 4.23$ MPa can be calculated by Eq. 21 and the harmonic (Reuss) mean

$$E_{1D} = \left(v_{inc} E_{inc}^{-1} + v_{matrix} E_{matrix}^{-1} \right)^{-1}. \tag{26}$$

Interestingly, the ratio $E_{1D}/E_{2D} \approx 0.82$ is close to $E_{2D}/E_{3D} \approx 0.79$. We will see that, as nice as this is, equating these ratios is in general not a good extrapolation strategy to obtain E_{3D} .

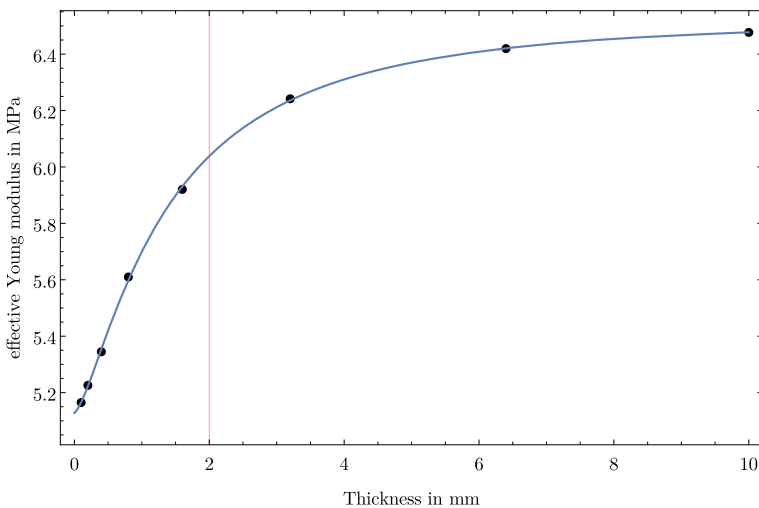


Fig. 8 Transition behavior as for the matrix inclusion structure with $K_{inc} = 10$, $G_{inc} = 10$, $K_{matrix} = 10$, $G_{matrix} = 1$ and $v_{inc} = 0.36$. The red line indicates the inclusion diameter

4.4.2 Patterns in E_{2D}/E_{3D}

We have already discussed that $E_{1D} < E_{2D} < E_{3D}$ holds. One might suspect that for a specific microstructure and material combination

$$\frac{E_{1D}}{E_{2D}} \approx \frac{E_{2D}}{E_{3D}} \tag{27}$$

may hold. However, this is not the case, as Fig. 9 makes clear. It may well happen that one of the values is around 0.2 while the other one is around 0.8. Nevertheless, patterns are visible. For some material parameter combinations, the volume fraction change along the dotted lines has a sickle shape, with the foam binary mixture near the cusp. Another way of looking at the data are histograms of the Young’s moduli ratios given in Fig. 10. One can see that the experimental value of 0.7 from Section 2 is a rather common value.

4.4.3 Load Redistribution Upon Slicing

In any case, the stress state is constrained to be plane in the slices, hence one dimension is not available for the load distribution, and the slices behave softer. Additionally, we observed a change of the microstructure topology in the foam structure. The slicing affects significantly the connectivity of the phases, which does not occur in the matrix-inclusion structure. The latter remains of matrix-inclusion type in the slices, while the foam structure tends to show inclusions in the slices while there are no inclusions in the bulk sample. This leads to a more pronounced strain concentration in the foam structure, see Fig. 11.

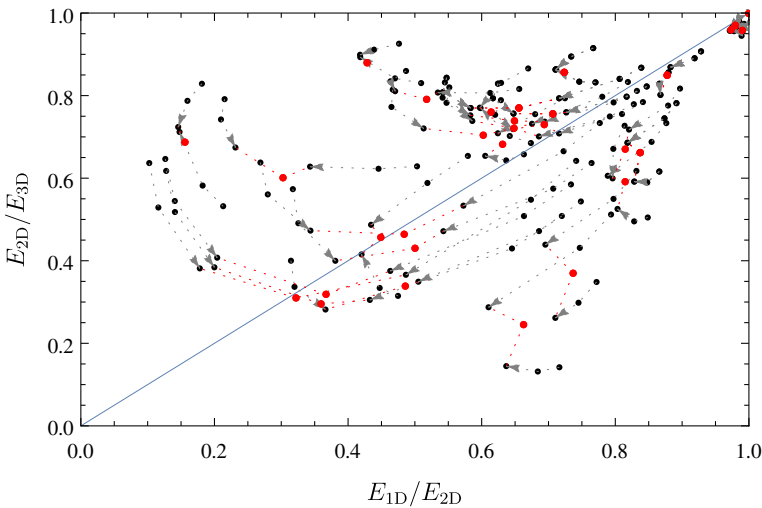


Fig. 9 Scattering of $\frac{E_{2D}}{E_{3D}}$ over $\frac{E_{1D}}{E_{2D}}$ for the 216 combinations of the matrix-inclusion structure (black dots) and the 36 combinations of the foam structure (red). Equal material parameter combinations are connected by dotted lines. For the matrix-inclusion structure, the arrows point in direction of the increasing volume fraction

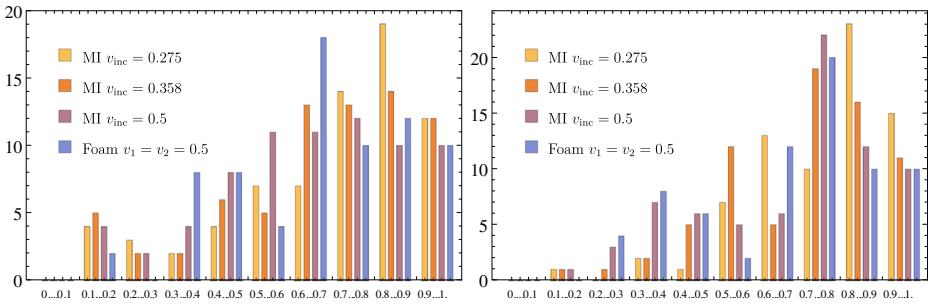


Fig. 10 Histograms of $\frac{E_{1D}}{E_{2D}}$ (left) and $\frac{E_{2D}}{E_{3D}}$ (right) for all simulations. The foam structure has been counted twice to account for the structural symmetry. One can see that the experimental value $\frac{E_{2D}}{E_{3D}} \approx 0.7$ is very typical

5 Regressions

To include the structural gradient in simulations of components, one is interested in the local 3D material properties. These are best obtained from statistically homogeneous bulk samples or RVE simulations. Unfortunately, homogeneous bulk samples of, e.g., only

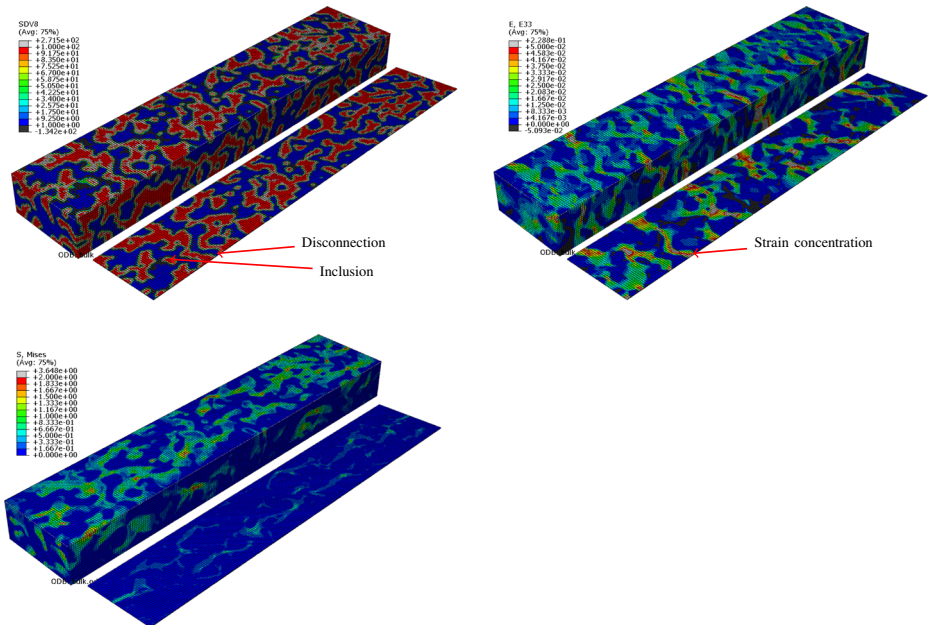


Fig. 11 Tensile test with the same prescribed nominal strain in the foam structure (top left) with the strain (right) and stress distributions (bottom). The slice corresponds to the top surface of the bulk, of which only the lower half is shown. One can see phase disconnections due to the slicing, which causes a strain concentration in the softer phase in the slice and hence lower stresses in the slice and therefore an overall softer response of the slice. The material parameters are $\nu_1 = \nu_2 = 0$, $E_1 = 1$ MPa, $E_1 = 100$ MPa. The effective properties are $E_{3D} \approx 19.9$ MPa, $E_{2D} \approx 5.16$ MPa, $E_{1D} = 1.98$ MPa

the casting skin, are not available, and RVE simulations require a 3D microstructure characterization, numerical effort and precise microscale modeling.

Therefore, we try to extrapolate to a local E_{3D} when only slices and the phase’s material parameters are available. E_{2D} is obtained from tensile tests on the slices and the phases elasticities are assumed to be given. We construct a regression on the synthetic data with the following properties:

- The regression has to be invariant under a change of the physical unit for the stiffness.
- It minimizes the relative error between the true value and the estimate.
- It uses only E_{2D} , the volume fractions and the phase’s elasticities as input.
- Its parameters are interpretable physically.
- It gives the exact result in the homogeneous case.

To comply with the first two requirements we formulate the regression in terms of the ratio of the increase of Young’s modulus. Further, we already found that the difference of the phase’s Poisson ratios plays a major role. The approach

$$\frac{E_{reg3D}}{E_{2D}} = \text{reg} \left(\Delta\nu, \frac{E_{2D}}{E_{1D}} \right) = 1 + p_\nu \Delta\nu^2 + p_E \left(\frac{E_{2D}}{E_{1D}} - 1 \right) \tag{28}$$

turned to give a reasonable regression with only two parameters p_ν and p_E , which both reflect a physical effect, as discussed later on. E_{1D} is obtained from the volume fractions and phase’s elasticities by Eq. (21). Further, one can see that the fifth requirement is met, i.e. in case of homogeneity we have $E_{2D}/E_{1D} = 1$ and $\Delta\nu = 0$, which yields $E_{reg3D}/E_{2D} = 1$.

The parameters p_ν and p_E have been adopted by a least square method. The result is plotted in Fig. 12 along with two automatic regressions. We tried different expressions, and found the t-test and significances where highest for the above approach. The t-test is approximately the ratio between the regression value and the standard error, and higher values indicate more significant contributions to the regressions. The values and their significances are given in Table 1. One can see that p_ν is more significant than p_E and similar in both structures, while p_E is three times larger in the foam structure. The reason for this is that p_ν captures the apparent softening due to free lateral contraction in the slices, for which the phase’s arrangement is not so important, but the difference between the Poisson ratios. On the other hand, p_E extrapolates the stiffness increase from 1D \rightarrow 2D to 2D \rightarrow 3D. As depicted in 11, additional dimensions allow for alternative load paths. While in both cases the load redistribution is significant when going from 1D to 2D, in the matrix-inclusion structure nothing new happens when going from 2D to 3D while new phase connections appear in this case in the foam structure. Thus, the extrapolation of Young’s moduli is more significant in the foam.

Table 1 Regression values for p_E and p_ν for both microstructures

		Value	Standard error	t-test	Significance
Matrix-inclusion	p_ν	0.753	0.05891	12.78	3.584×10^{-28}
	p_E	0.09394	0.03013	3.085	0.002305
Foam	p_ν	0.6188	0.1527	4.052	0.0002792
	p_E	0.2842	0.108	2.631	0.01272

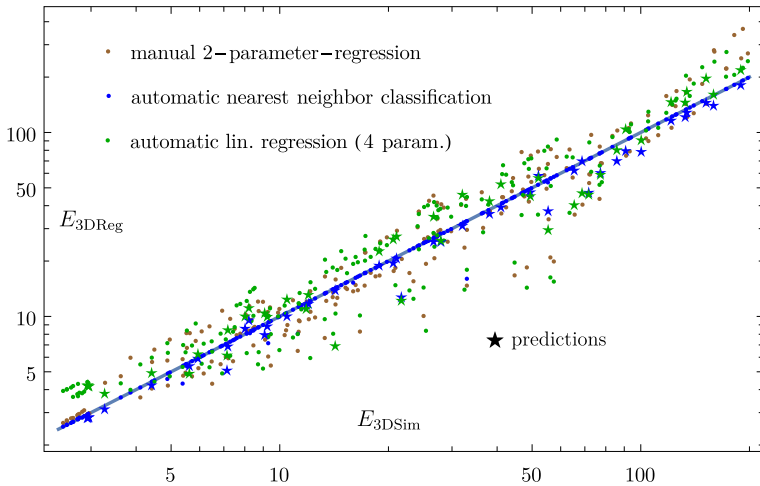


Fig. 12 The predicted E_{3DReg} from the regression over the actual E_{3DSim} . Double logarithmic axes are chosen to visualize the uniform relative error. The manual 2-parameter-regression performs as good as automatic regressions. Ideally, all points would lie on the diagonal

It is surprising how well the manual regression compares to automatic regressions that have been obtained with a computer algebra system, as shown in Fig. 12. For the automatic regressions the set was split into training set (80%) and a test set (20%).

6 2D to 3D Transition by Lateral Confinement Relaxation

The above results bear the question of how one can account for the difference between plane and 3D stiffnesses using well-established models. We want to present a simple scheme how at least the 2D to 3D- lateral confinement effect can be quantified.

The free lateral straining in plane stress states can be approximately accounted for by matching the phases’ Poisson’s ratios. Assuming a given estimate of the 3D stiffness properties of a two phase composite with isotropic phases with material parameters $E_{1,2}, \nu_{1,2}$, a relaxation of the stress field from 3D to 2D can be mimiced by matching ν_1 and ν_2 . A simple approach is to replace ν_1 and ν_2 in the 3D estimate by the average $\bar{\nu} = \nu_1 \nu_1 + \nu_2 \nu_2$. A comparison of the original 3D estimate and the relaxed version gives an estimate on how much the effective tensile moduli differ in the slice and the bulk material. Especially, the ratio E_{2D}/E_{3D} can be given as a function of volume fractions and material parameters. The microstructure morphology is accounted for by selecting the 3D estimate. We expect this to work reasonably well in matrix-inclusion-structures, as these remain matrix-inclusion structures when they are sliced. Therefore, we consider the Mori-Tanaka-approach [17]. It is relatively simple and works well for small volume fractions and not too large phase contrasts. For an isotropic matrix and isotropic spherical inclusions we have

$$\bar{G}_{MT} = \frac{G_{mat}(G_{inc}(8G_{mat}\nu_{inc} + 12G_{mat} + 9K_{mat}\nu_{inc} + 6K_{mat})) + G_{mat}\nu_{mat}(8G_{mat} + 9K_{mat})}{G_{mat}(6\nu_{inc}(2G_{mat} + K_{mat}) + 8G_{mat} + 9K_{mat}) + 6G_{inc}\nu_{mat}(2G_{mat} + K_{mat})} \tag{29}$$

$$\bar{K}_{MT} = \frac{4G_{matrix}(K_{inc}\nu_{inc} + K_{matrix}\nu_{matrix}) + 3K_{inc}K_{matrix}}{4G_{matrix} + 3(K_{inc}\nu_{matrix} + K_{matrix}\nu_{inc})} \tag{30}$$

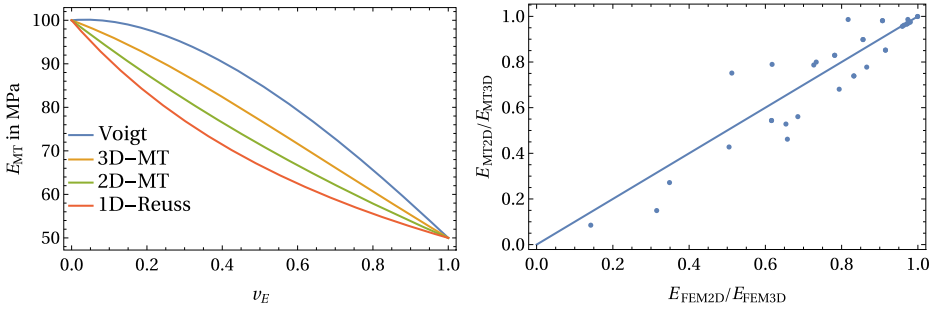


Fig. 13 Left: Comparison of the 3D- and plane stress-relaxed (2D) Mori-Tanaka approaches along with the 3D Voigt-Reuss-bounds. Right: Comparison of the ratios E_{2D}/E_{3D} for the Mori-Tanaka-estimates and the simulation results. We have restricted this comparison to the case $\nu_{inc} = 0.275$ and $1/5 < E_{matrix}/E_{inc} < 5$, since the Mori-Tanaka estimate gives only for small volume fractions and small phase contrasts reasonable results

With the conversion Eqs. (21) to (24) the estimates can be recast as

$$E_{MT}(E_{inc}, E_{matrix}, \nu_{inc}, \nu_{matrix}). \tag{31}$$

A plane stress, 2D-estimate with free lateral contraction is obtained by replacing $\nu_{matrix}\nu_{matrix} + \nu_{inc}\nu_{inc}$ in the last two entries of Eq. (31). We have plotted the result for an example material $E_{matrix} = 100$ MPa, $E_{inc} = 50$ MPa, $\nu_{matrix} = 0$, $\nu_{inc} = 0.4$ in Fig. 13 left.

One can see that $q = E_{MT2D}/E_{MT3D}$ can be estimated. Simple tests of plausibility hold: $q = 1$ for $\nu_{inc} = \nu_{matrix}$, $q < 1$ for $\nu_{inc} \neq \nu_{matrix}$ or $\nu_{matrix} \neq \nu_{inc}$, where for extreme differences the relaxed MT-estimate approaches the lower Reuss bound, i.e. the 1D-stiffness. Moreover we have $E_{1D} = E_{Reuss} \leq E_{MT2D} \leq E_{MT3D} \leq E_{Voigt}$, i.e. the correct ordering is obtained. Figure 13 right shows the quality of the estimate of the Young’s moduli ratios for plane stress and 3D tests with $\nu_{inc} = 0.275$ and for all simulations with $1/5 < E_{matrix}/E_{inc} < 5$. The Poisson’s ratios are in the interval $-0.96 < \nu < 0.495$, where the largest difference is $|\nu_E - \nu_M| \approx 1.45$. One can see that the predictive capability of the simple relaxation is not too bad, even for large reductions of stiffness and in view of the large differences of Poisson-ratios and the moderate quality of the Mori-Tanaka approach. For larger volume fractions and phase contrasts the quality deteriorates quickly. Especially for polymeres with $E_{crystalline}/E_{amorphous} \approx 10^3$ and volume fractions $\nu_{crystalline} \approx 0.4 \dots 0.6$ better approaches are needed.

Nevertheless, the relaxation has the advantage that it can be applied to existing 3D estimates, as long as these can be recast in terms of the phase’s Poisson ratios. It should further also be possible to employ such a relaxation in the anisotropic case.

7 Summary

We have discussed the stiffness reduction as encountered when materials with microstructures are subjected to tensile tests as bulk and sliced samples, and have given two real world examples. The lower Young modulus of the sliced sample is the consequence of a lack of scale separation along the slice normal and a confinement to the plane stress state. The direction normal to the slice is not available for load distribution. Analysing the phenomenon with

synthetic data, we were able to identify the contributions to the stiffness reduction. The first contribution is the free lateral straining in tensile tests in slices, which is more significant the bigger the difference of the phase's Poisson's ratios is. For the latter effect, we propose a relaxation scheme that simply mimics the free lateral contraction by matching the Poisson ratios. The latter approach can be applied to any 3D estimate that can be recast in terms of the Poisson's ratios of the phases. The second effect, namely topological changes upon slicing, is harder to account for. A 3D-microstructure with interpenetrating phases shows characteristics of a matrix-inclusion structure when slices are considered. This results in a considerable load path change from the 3D to the 2D case.

We believe to only have scratched the surface of this interesting and apparently not much appreciated phenomenon, which is worth more attention. For example, grain structures have not been considered here. Possible benefits from further investigations include

- more precise material characterizations when structural gradients are present,
- extrapolations from 2D to 3D may allow for approaching the 3D properties from representative area elements with less numerical effort,
- technological use of the possibly drastic reduction of stiffness when going from bulk to slice structures.

Acknowledgements Rainer Glüge gratefully acknowledges funding under research project *Controlling crystallization as a strategy to improve injection molded components* from the European Union from the European Regional Development Fund (ERDF 2016-2019) under research grant no. EFRE 11.000sz00.00.0.16.106680.0.

Funding Open Access funding enabled and organized by Projekt DEAL.

Open Access This article is licensed under a Creative Commons Attribution 4.0 International License, which permits use, sharing, adaptation, distribution and reproduction in any medium or format, as long as you give appropriate credit to the original author(s) and the source, provide a link to the Creative Commons licence, and indicate if changes were made. The images or other third party material in this article are included in the article's Creative Commons licence, unless indicated otherwise in a credit line to the material. If material is not included in the article's Creative Commons licence and your intended use is not permitted by statutory regulation or exceeds the permitted use, you will need to obtain permission directly from the copyright holder. To view a copy of this licence, visit <http://creativecommons.org/licenses/by/4.0/>.

References

1. Adams, B.L., et al.: *Microstructure Sensitive Design for Performance Optimization*. Elsevier Science (2012)
2. Bendsøe, M.P., Kikuchi, N.: Generating optimal topologies in structural design using a homogenization method. *Comput. Methods Appl. Mech. Eng.* **71.2**, 197–224 (1988)
3. Brannon, R.M.: *Rotation, Reflection, and Frame Changes*. IOP Publishing (2018)
4. Eidel, B. et al.: Estimating the effective elasticity properties of a diamond/ β -sic composite thin film by 3D reconstruction and numerical homogenization. *Diamond and Related Materials* **97**, 107406 (2019)
5. Francfort, G., Murat, F.: Homogenization and optimal bounds in linear elasticity. *Archive for Rational Mechanics and Analysis* **94.4**, 307–334 (1986)
6. Geoffroy-Donders, P., et al.: 3-d topology optimization of modulated and oriented periodic microstructures by the homogenization method. *J. Comput. Phys.* **401**, 108994 (2020)
7. Glüge, R.: Generalized boundary conditions on representative volume elements and their use in determining the effective material properties. *Comput. Mater. Sci.* **79**, 408–416 (2013)
8. Hencky, H.: Zur Theorie plastischer Deformationen und der hierdurch im Material hervorgerufenen Nachspannungen. *Zeitschrift für angewandte Mathematik und Mechanik* **4**, 323–334 (1924)

9. Horváth, Z., et al.: Effect of molecular architecture on the crystalline structure and stiffness of iPP homopolymers: Modeling based on annealing experiments. *J. Appl. Polymer Sci.* **130.5**, 3365–3373 (2013)
10. Huang, L., Geng, L.: *Discontinuously Reinforced Titanium Matrix Composites: Microstructure Design and Property Optimization*. Springer, Singapore (2017)
11. Hwang, S.-G.: Cauchy's interlace theorem for eigenvalues of hermitian matrices. *The American Mathematical Monthly* **111.2**, 157–159 (2004)
12. Hyde, J.M. et al.: Modelling spinodal decomposition at the atomic scale: beyond the Cahn - Hilliard model. *Model. Simulation Mater. Sci. Eng.* **4.1**, 33–54 (1996)
13. Ilyushin, A.A.: Theory of plasticity at simple loading of the bodies exhibiting plastic hardening. *Rossiiskaya Akademiya Nauk (Prikl Mat. Mekh.)* **11**, 291 (1947)
14. Lin, Y. et al.: Mechanical properties and optimal grain size distribution profile of gradient grained nickel. *Acta Mater.* **153**, 279–289 (2018)
15. Mahmood, N. et al.: Influence of structure gradients in injection moldings of isotactic polypropylene on their mechanical properties. *Polymer* **200**, 122556 (2020)
16. Mandel, J.: Generalisation de la theorie de plasticite de W. T. Koiter. *International Journal of Solids and Structures* **1.3**, 273–295 (1965)
17. Mori, T., Tanaka, K.: Average stress in matrix and average elastic energy of materials with mifitting inclusions. *Acta Metallurgica* **21.5**, 571–574 (1973)
18. Quayum, S., et al.: Computational model generation and RVE design of self-healing concrete. *Frontiers of Structural and Civil Engineering* **9(4)**, 383–396 (2015)
19. Ramberg, W., Osgood, W.R.: Description of stress-strain curves by three parameters. *Technical Note* **902**, 1–28 (1943)
20. Reuss, A.: Berechnung der fließgrenze von Mischkristallen auf Grund der plastizitätsbedingung für Einkristalle. *ZAMM - Journal of Applied Mathematics and Mechanics / Zeitschrift für Angewandte Mathematik und Mechanik* **9.1**, 49–58 (1929)
21. Thomson, W.: XXI. Elements Of a mathematical theory of elasticity. *Philos. Trans. R. Soc. Lond.* **146**, 481–498 (1856)
22. Tordjeman, Ph., et al.: The effect of α , β crystalline structure on the mechanical properties of polypropylene. *European Phys. J. E* **4.4**, 459–465 (2001)
23. Torquato, S.: Effective stiffness tensor of composite media. Exact series expansions. *J. Mech. Phys. Solids* **45.9**, 1421–1448 (1997)
24. Voigt, W.: *Lehrbuch Der Kristallphysik*. B. G. Teubners Sammlung von Lehrbüchern auf d. Geb. d. math. Wiss. Johnson Reprint Corporation (1928)

Publisher's Note Springer Nature remains neutral with regard to jurisdictional claims in published maps and institutional affiliations.